

Numerical Investigation of Bioinspired Blade Designs at High Reynolds Numbers for Ultra-Quiet Aircraft and Wind Turbines

Andrew Bodling^{*}, Bharat Raj Agrawal[†], Anupam Sharma[‡]

Department of Aerospace Engineering, Iowa State University, Ames, IA, USA, 50011.

Ian Clark[§], W. Nathan Alexander[¶] and, William Devenport^{||}

Department of Aerospace and Ocean Engineering,

Virginia Polytechnic Institute and State University, Blacksburg, VA, 24061.

This paper presents numerical analysis of an airfoil geometry inspired by the down coat of the night owl. The objective is to understand the mechanisms of airfoil trailing edge noise reduction that has been observed with such designs in previous experiments. The NACA 0012 airfoil is selected as the baseline airfoil. The bioinspired geometry consists of an array of “finlets” that are applied near the trailing edge of the baseline airfoil and are aligned with the flow direction. Wall-resolved large eddy simulations (LES) are performed over the baseline and the bioinspired airfoil geometries and the aerodynamic and aeroacoustic performance of the two geometries are contrasted. Both models are simulated at chord-based Reynolds number $Re_c = 5 \times 10^5$, flow Mach number, $M_\infty = 0.2$, and angle of attack, $\alpha = 0^\circ$. The simulations are tripped in order to compare with experiments that are at much higher Re_c (of the order of 2 M). Tripping is achieved using a geometry-resolved trip wire, placed at $x/c = 0.05$ from the airfoil leading edge. Comparisons with experimental data show good agreement for aerodynamic pressure coefficient (C_p) distribution for the baseline airfoil. Skin friction coefficient (C_f) and C_p distributions are also found to compare well with XFOIL results obtained by similarly tripping the boundary layer. Surface pressure spectra

^{*}Graduate student, 1200 Howe Hall, Ames IA, 50011. abodling@iastate.edu. AIAA Student Member

[†]Ph.D. student, 1200 Howe Hall, Ames IA, 50011. bharatr@iastate.edu. AIAA Student Member.

[‡]Assistant Professor, 2341 Howe Hall, Ames, IA, 50011. sharma@iastate.edu. AIAA Senior Member.

[§]Ph.D. student, clarki91@vt.edu. AIAA Student Member.

[¶]Assistant Professor, alexande@vt.edu. AIAA Member.

^{||}Professor, McBryde Hall, RM 660E, 225 Stanger St., Blacksburg, VA 24061. devenport@vt.edu. AIAA Associate Fellow.

comparisons between the baseline and the bioinspired airfoil near the airfoil trailing edge show reductions with the finlets of the order of 3 dB at high frequencies. Two hypotheses of noise reduction mechanisms are investigated: (1) reduction in spanwise correlation length, and (2) increase in source-’scattering edge’ separation distance. The simulations show insignificant difference in spanwise coherence between the two geometries, but clearly show that the finlets lift turbulence eddies away from the airfoil trailing edge hence reducing scattering efficiency.

I. Introduction

The continued growth in wind energy and air travel is exacerbating the associated noise pollution problem. Noise can have detrimental effects to human health, which are well documented.¹⁻⁵ Research in the area of noise reduction is therefore critical for the development of future aircraft and wind turbines. Biomimicry has resulted in many engineering innovations.⁶ One biological feature that has yet to be used in engineering innovations is the silent flight of nocturnal owls. The nocturnal owl can not be heard until it is within 3 meters.⁷ One species of nocturnal owls - the barn owl (*Tyto alba*) - is particularly adept at silent flight. In this paper, we refer to the barn owl as ‘the owl’.

The owl has three unique feather features that are believed to contribute to its nearly silent flight. These are: (1) leading edge comb (or serrations), (2) trailing edge fringe, and (3) down coat on flight feathers. Figure 1 highlights these unique feather features using images of barn owl wing specimens. Previous studies (see e.g.,⁸⁻¹⁵) have investigated blade designs inspired by the owl leading edge comb and trailing edge fringe. The studies have used numerical, analytical, and experimental methods, even including demonstrations on full-scale, field tests.¹⁶ The down coat has also been investigated analytically^{17,18} and experimentally.¹⁹⁻²¹ However, little to no numerical research investigating the acoustic impact of the owl down coat has been performed. This paper aims to fill this technical void through detailed flow and sound source diagnostics performed using highly-resolved large-eddy simulations.

It should be noted that the chord-based Reynolds number for the owl in gliding flight is between 50,000 – 90,000. Figure 2 illustrates the range of Reynolds number over which various flying machines and animals, including the owl, operate. The goal of this paper however, is to investigate blade designs that can reproduce the silencing feature of the owl at a much higher Reynolds number (of the order of a few million), which is relevant to wind energy and aerospace engineering applications. We therefore aim for bioinspiration and not biomimicry.

The particular bioinspired blade designs that form the focus of this paper were first discussed by Clark *et al.*¹⁹ They suggested that the down coat (made of hairs that rise up vertically and plateau in the flow direction) forms a “canopy” and makes the flow behave similar to forest canopy flows. They attempted to

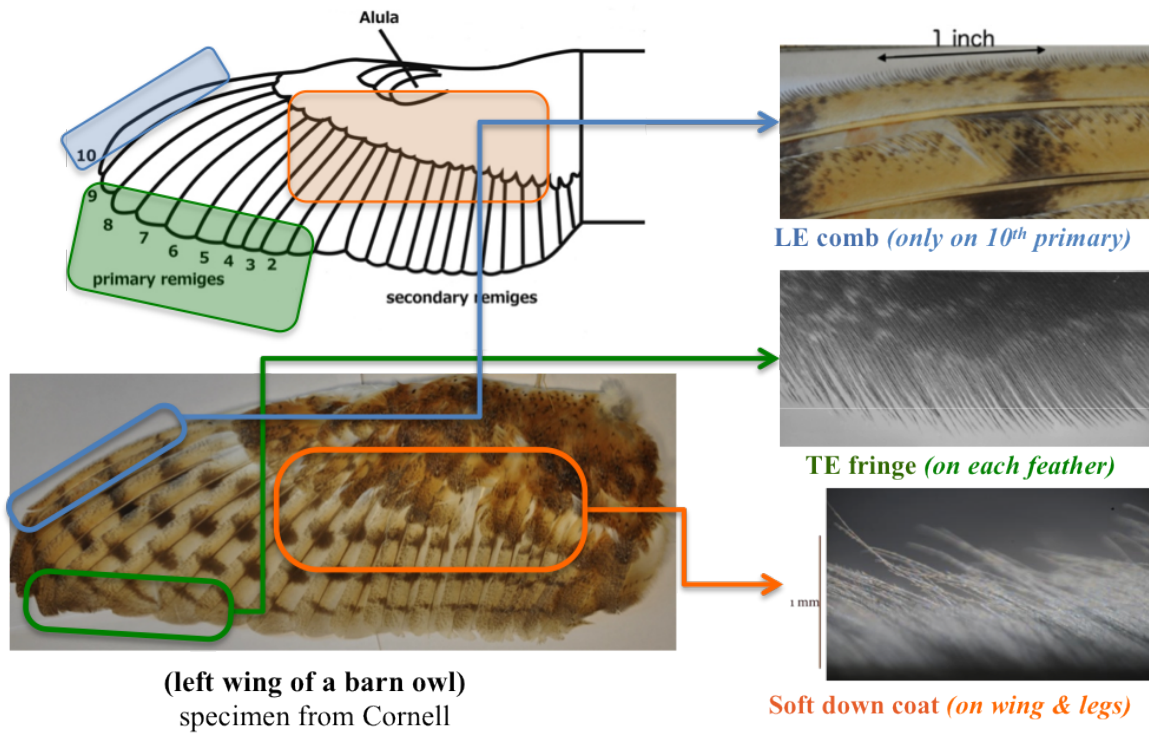


Figure 1. The owl hush kit: unique feather adaptations that enable the owl to fly silently. Top: barn owl wing specimen. Bottom: Photographs through a microscope of (a) leading edge comb, (b) down coat on flight feathers, and (c) trailing edge fringe. Images (b) and (c) are from Refs.^{7,19}

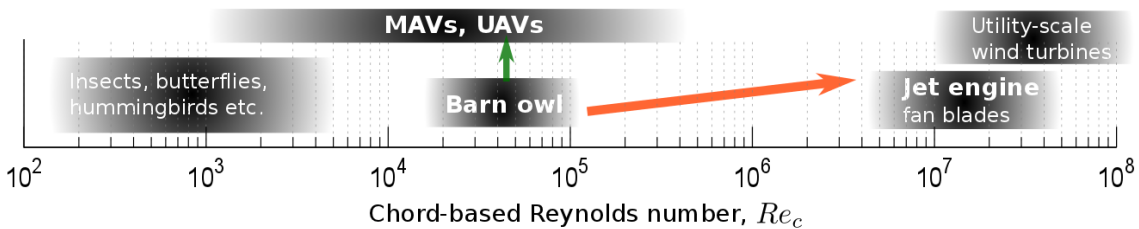


Figure 2. Chord based Reynolds number of various species compared with different aircraft

reproduce this canopy effect using “finlets” which were constructed in two different ways - (a) using an array of sharp edge fences, and (b) using tiny cylindrical rails. Clark *et al.*^{19,20} presented aeroacoustics measurements of trailing edge noise from airfoils with these finlets (fences and rails) installed using a substrate near the trailing edge of the baseline airfoil. The DU96-W-180 airfoil, commonly used in wind turbine applications, was selected as the baseline.

Figure 3 shows schematics of the two finlet designs used in the experiments. Plots (a) and (b) in the figure are the fence and rail configurations, respectively. Farfield sound was measured using acoustic beamforming²² and the finlet designs were found to be significantly quieter than the baseline airfoil.²⁰ The tests were conducted at very low Mach numbers with minimal inflow turbulence and at angles of attack

where the airfoil boundary layer does not separate. The primary mechanism of noise generation under these conditions is scattering of the hydrodynamic energy in the boundary layer turbulence by the airfoil trailing edge.

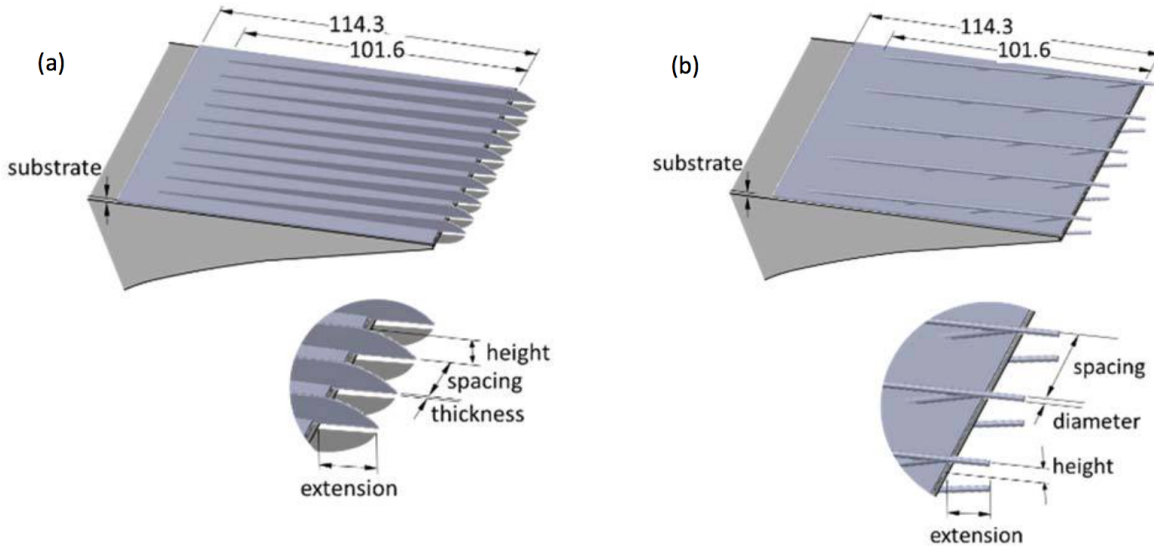


Figure 3. Schematics of two finlet designs used by Clark *et al.*²⁰

This paper presents results of highly-resolved large eddy simulations of a baseline airfoil as well as the baseline airfoil fitted with finlet fences. The baseline airfoil selected for this study is NACA-0012, which is different from the experiments.²⁰ Furthermore, the simulations are performed at a much smaller Reynolds number compared to the experiments – 5×10^5 versus 2.1×10^6 . These simplifications are made to manage the computational complexity of the problem. Nevertheless, the simulations reveal several interesting flow physics that shed new light on the potential mechanisms of the observed noise reduction, thus supplementing the experimental results of Ref.²⁰ Results from two sets of simulations are presented: (a) baseline airfoil (NACA-0012), and (b) NACA-0012 with a modified version of one of the finlet fence designs of Ref.²⁰ The objective here is to make *qualitative* comparisons between the simulations and experiments to gain confidence in the simulations, and then perform source diagnostics using the highly-resolved flowfield to enhance our understanding of the noise reduction mechanisms with the finlet design.

II. Numerical Methodology

The compressible Navier-Stokes solver, FDL3DI,²³ is used for the fluid flow simulations. The governing fluid flow equations (solved by FDL3DI), after performing a time-invariant curvilinear coordinate transform

$(x, y, z, t) \rightarrow (\xi, \eta, \zeta, \tau)$, are written in a strong conservation form as

$$\frac{\partial}{\partial t} \left(\frac{\mathbf{U}}{J} \right) + \frac{\partial \hat{\mathbf{F}}_I}{\partial \xi} + \frac{\partial \hat{\mathbf{G}}_I}{\partial \eta} + \frac{\partial \hat{\mathbf{H}}_I}{\partial \zeta} = \frac{1}{Re} \left[\frac{\partial \hat{\mathbf{F}}_v}{\partial \xi} + \frac{\partial \hat{\mathbf{G}}_v}{\partial \eta} + \frac{\partial \hat{\mathbf{H}}_v}{\partial \zeta} \right], \quad (1)$$

where $J = \partial(\xi, \eta, \zeta, \tau)/\partial(x, y, z, t)$ is the Jacobian of the coordinate transformation, $\mathbf{Q} = \{\rho, \rho u, \rho v, \rho w, \rho E\}$; the inviscid flux terms, $\hat{\mathbf{F}}_I, \hat{\mathbf{G}}_I, \hat{\mathbf{H}}_I$ are

$$\hat{\mathbf{F}}_I = \begin{bmatrix} \rho \hat{U} \\ \rho u \hat{U} + \hat{\xi}_x p \\ \rho v \hat{U} + \hat{\xi}_y p \\ \rho w \hat{U} + \hat{\xi}_z p \\ (\rho E + p) \hat{U} - \hat{\xi}_t p \end{bmatrix}, \quad \hat{\mathbf{G}}_I = \begin{bmatrix} \rho \hat{V} \\ \rho v \hat{V} + \hat{\eta}_x p \\ \rho w \hat{V} + \hat{\eta}_y p \\ \rho w \hat{V} + \hat{\eta}_z p \\ (\rho E + p) \hat{V} - \hat{\eta}_t p \end{bmatrix}, \quad \text{and} \quad \hat{\mathbf{H}}_I = \begin{bmatrix} \rho \hat{W} \\ \rho u \hat{W} + \hat{\zeta}_x p \\ \rho v \hat{W} + \hat{\zeta}_y p \\ \rho w \hat{W} + \hat{\zeta}_z p \\ (\rho E + p) \hat{W} - \hat{\zeta}_t p \end{bmatrix}, \quad (2)$$

where,

$$\begin{aligned} \hat{U} &= \hat{\xi}_t + \hat{\xi}_x u + \hat{\xi}_y v + \hat{\xi}_z w, \\ \hat{V} &= \hat{\eta}_t + \hat{\eta}_x u + \hat{\eta}_y v + \hat{\eta}_z w, \\ \hat{W} &= \hat{\zeta}_t + \hat{\zeta}_x u + \hat{\zeta}_y v + \hat{\zeta}_z w, \quad \text{and} \\ \rho E &= \frac{p}{\gamma - 1} + \frac{1}{2} \rho (u^2 + v^2 + w^2). \end{aligned} \quad (3)$$

In the above, $\hat{\xi}_{(x,y,z)} = J^{-1} \partial \xi / \partial (x, y, z)$, and u, v, w are the components of the velocity vector in Cartesian coordinates, and ρ, p, T are respectively the fluid density, pressure, and temperature. The gas is assumed to be perfect, $p = \rho T / \gamma M_\infty^2$. The viscous flux terms, $\hat{\mathbf{F}}_v, \hat{\mathbf{G}}_v, \hat{\mathbf{H}}_v$ are provided in Ref.²⁴

We perform *implicit* large eddy simulations (ILES) simulations by filtering the solution at every sub-iteration using an eighth-order, low-pass spatial filter. The numerical schemes uses compact finite differences with a sixth-order spatial accuracy, and time integration is performed using an approximately factored, second order implicit Beam-Warming scheme.

III. Geometry Modeling, Meshing, and Boundary Conditions

The NACA-0012 airfoil is selected as the baseline airfoil. For the bioinspired airfoil, finlet fences are added near the trailing edge. The span length of the airfoil model in the simulations is 5.85% of the airfoil chord. A single-block, O-grid is used to generate a 2-D mesh around the baseline airfoil, which is repeated in the span direction to obtain the 3-D grid. The O-grid in the physical space (x, y, z) maps to an H-grid in the computational domain (ξ, η, ζ) . The following orientation is used: \hat{e}_ξ points radially out, \hat{e}_η is in

the circumferential direction. \hat{e}_ζ is along the span direction such that the right hand rule, $\hat{e}_\zeta = \hat{e}_\xi \times \hat{e}_\eta$ is obeyed.

Periodicity is imposed in the span direction (\hat{e}_ζ). Periodic boundary conditions are implemented using the Overset grid approach in FDL3DI. A minimum of five-point overlap is required by FDL3DI to ensure high-order accurate interpolation between individual meshes. The airfoil surface is modeled as a no-slip, adiabatic wall. Freestream conditions are prescribed at the outer boundary and the grid is coarsened away from the airfoil surface in order for the filtering procedure to dissipate all perturbations from the flow before they reach the outer boundary.

A. Baseline Airfoil Mesh

The baseline is the NACA-0012 airfoil with a rounded trailing edge. The simulations are carried out at chord-based Reynolds number, $Re_c = 500,000$, angle of attack, $\alpha = 0^\circ$, and flow Mach number, $M_\infty = 0.2$. The choice of the first cell height with these flow conditions gives an average $y^+ \approx 0.279$ for the baseline geometry. Figure 4 shows close-up, cross-sectional views of the baseline O-grid. Table 1 provides the metrics of the grid used for the baseline simulation.

Table 1. Baseline grid metrics used for the $Re_c = 5 \times 10^5$, $AOA = 0^\circ$, forced transition simulation.

N_ξ	N_η	N_ζ	avg y^+	avg x^+	avg z^+	max y^+	max x^+	max z^+
410	1937	101	0.279	10.87	7.91	0.46	16.71	14.10

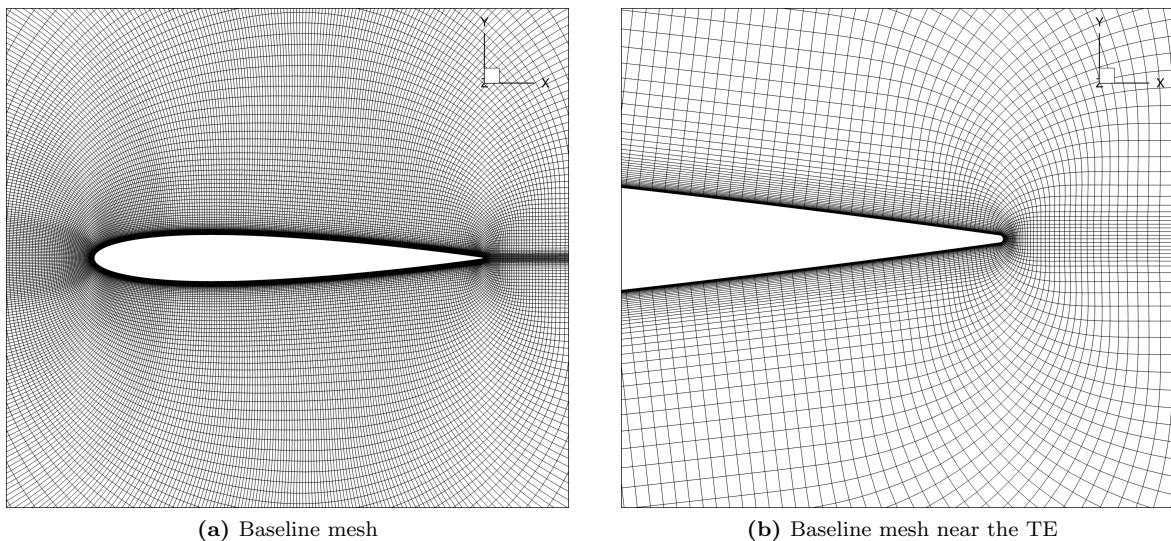


Figure 4. O-grid topology of the baseline mesh used in simulation #3. The trailing edge is rounded off and the mesh near the TE is shown in (b). Every 4th point along each axis is shown for clarity.

B. Finlet Fence Geometry and Mesh

Figure 5 contrasts the geometry of the fences between experiments and simulations. The major difference between the way the geometry is modeled in the simulations is the leading edge of the fence, which is nearly parallel to the flow in the experiments but almost orthogonal to the flow in the simulation. The reason for having this orthogonal edge in the simulations is that the mesh for the fence geometry is obtained directly from the baseline mesh by blanking out a subset of cells defined by specifying ranges of the coordinates ξ, η, ζ . No-slip wall boundary condition is applied on the fence boundaries obtained from grid-point blanking. This difference in the fence geometry between the experiments and the simulation has important aeroacoustic consequences. The orthogonal sharp leading edge of the fences in the simulations is a very efficient scatterer of the hydrodynamic energy in the incoming turbulence in the surface boundary layer. The trace velocity of the hydrodynamic perturbations along the orthogonal (to the flow) fence edge is infinite, which makes the scattering process very efficient. In the experiments, the leading edge of the fences is nearly tangential to the flow, making the trace velocity of the hydrodynamic perturbations along the edge highly subsonic, thereby rendering it inefficient in scattering. This extraneous source of noise in the simulations can potentially offset the benefit of reduced trailing edge noise with fences. Another potential problem with the orthogonal leading edge is that it can act as a turbulence (and hence noise) generator.

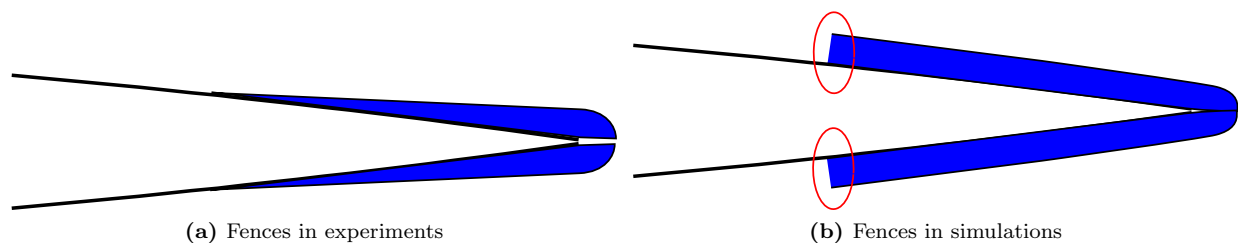


Figure 5. Schematics highlighting the differences in fence geometries between the experiments and FDL3DI computations.

The dimensions of the finlet fence are similar to configuration # 13 in the experiments of Ref.²⁰ Figure 6 show cross-sectional views of the finlet fence mesh. Figure 7 compares top views of the baseline mesh and the fence mesh, zooming in on one fence element. The ‘single fence element’ mesh is repeated several times along the span to obtain a 3-D mesh with a span of 5.85% chord. It should be emphasized that other than the holes (point blanking) introduced in the fence mesh, the grids between the baseline and the fence cases are identical. This eliminates grid-to-grid differences in the simulation results when comparing the two airfoil designs.

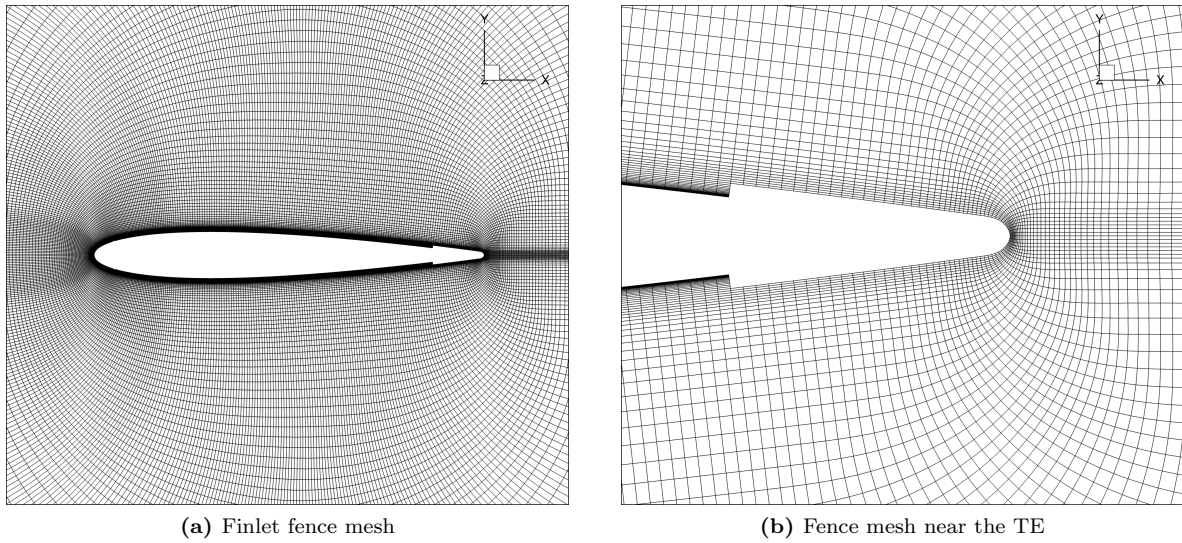


Figure 6. Cross sectional views of the computational mesh used to simulate the finlet fence geometry. Every 4th grid point along each axis is shown for clarity.

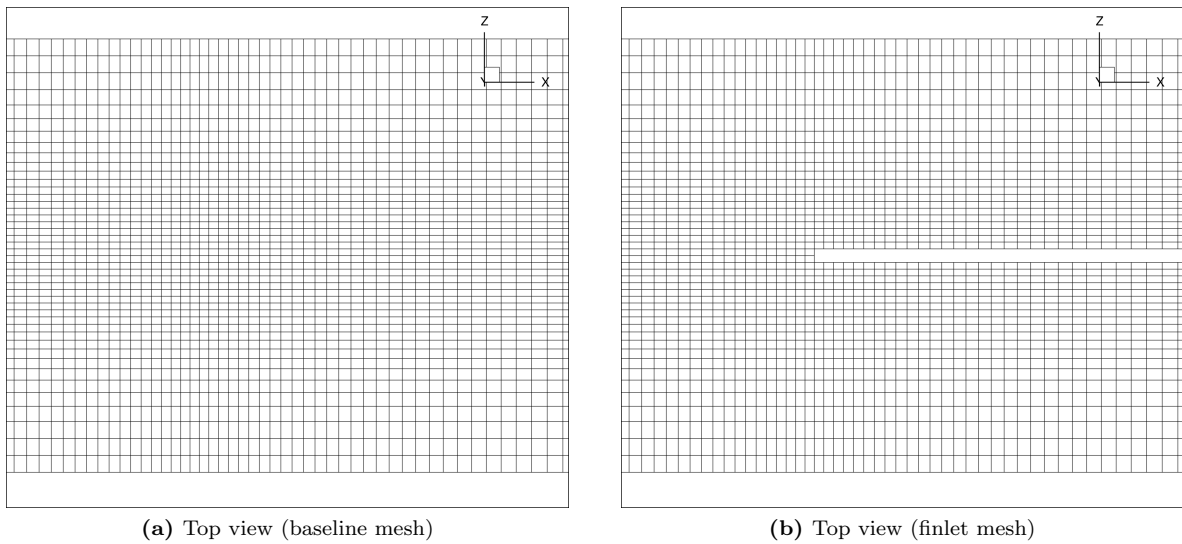


Figure 7. Top views of the baseline and fence meshes. Each fence element is modeled to be two cells thick in the simulations.

IV. Results

This section presents the results of the numerical simulations followed by a discussion about noise reduction mechanisms with the finlet design.

A. Boundary Layer Trip

Since the simulation $Re_c (= 5 \times 10^5)$ is much smaller than that of the experiments ($\approx 2 \times 10^6$), the boundary layers on the airfoil surfaces are tripped in the simulations. It should be noted that the boundary layer was also tripped in the experiments using a serrated tape. In the simulations, boundary layer tripping is achieved by placing a geometry-resolved “trip wire” at $x/c = 0.05$, measured from the leading edge of the airfoil. The trip wire is a square cylinder that extends throughout the span and is defined by blanking out cells in the regions occupied by the wire (see Fig. 8). The dimensions of the wire are defined by specifying ranges of the grid indices in the ξ, η , & ζ directions; no-slip wall boundary condition is applied to the boundaries of the trip wire. Figure 9 shows iso-surfaces of Q -criterion ($Q = 50$) on the suction surface of the baseline

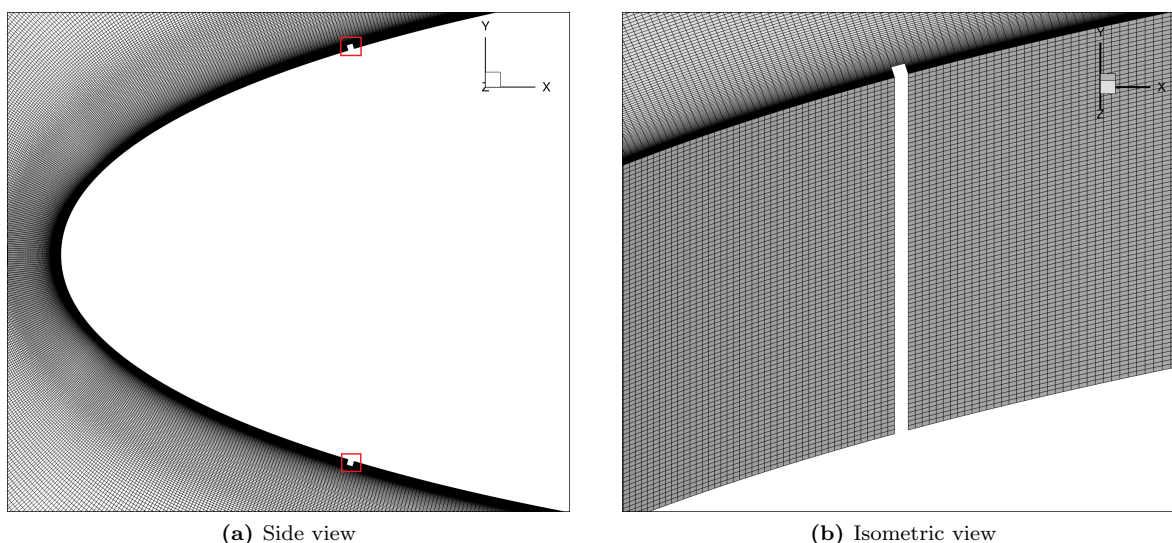


Figure 8. Mesh points that are blanked out to simulate boundary layer trip wires (locations indicated with red squares in (a)). The nodes adjacent to the blanked-out points are assigned the no-slip boundary condition. The trip wires span the entire span length of the computational domain.

airfoil for two cases: (a) natural transition, and (b) forced transition with the trip wire in place. The trip wire successfully forces the boundary layer to transition well upstream, compared to where it transitions naturally, thereby achieving a turbulent boundary layer similar to what would occur via natural transition at high Re_c .

B. Removal of Transients

Several techniques are employed to reduce the computational cost of the simulations. Each simulation is initiated in 2-D, with a potential flow solution as the initial condition. The Navier-Stokes equations are then solved for the 2-D problem until statistical convergence is achieved; this typically takes about $10 \times \tau$, where $\tau (= c/u_\infty)$ is the characteristic flow time. The solution is then replicated in the span direction to

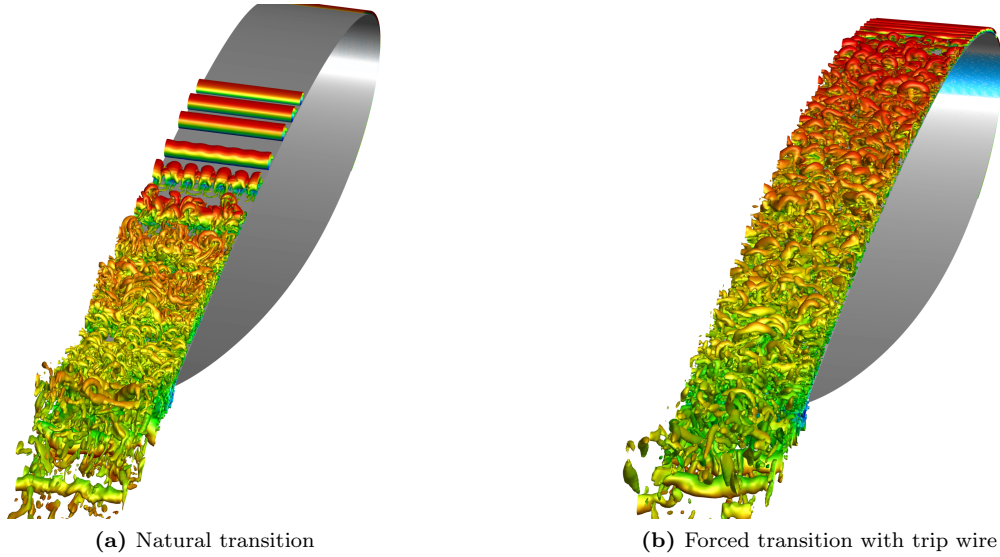


Figure 9. Iso-surfaces of the Q-criterion ($Q = 50$) comparisons of a) natural boundary layer transition and b) forced boundary layer transition.

obtain an initial 3-D solution for the baseline geometry. Transients in the 3-D simulation are then removed, which takes between $3\tau - 5\tau$. For the 3-D simulations with fences, the 3-D solution is obtained in two steps. First the 2-D solution is replicated over a single-fence span width and simulated with the fences modeled in the computation, and the solution is allowed to reach statistical stationarity ($\approx 5\tau$). This solution is then repeated for as many fences as required to fit in the 5.95% span length of the full 3-D geometry simulated. Transients are then removed in the full 3-D simulation (with the array of fences) by simulating the flow for another 5τ .

C. Aerodynamic Performance Results

Once the transients are removed from the 3-D simulations, the simulation data is averaged in time for approximately $2 \times \tau$ to obtain aerodynamic performance predictions. Time-averaged flow data is further averaged in span to compare against experiments as well as against XFOIL results. XFOIL²⁵ is a panel method code that simultaneously solves potential flow equations with boundary integral equations. Natural boundary layer transition in XFOIL is determined using the e^N linear stability method. For alternate transition mechanisms, boundary layer trips are set up in XFOIL.

1. Baseline Results Compared with Measurements

Figure 10 (a) compares the predicted time- and span-averaged aerodynamic pressure coefficient (C_p) distributions for the baseline airfoil with experimental data as well as with XFOIL predictions. The experimental measurements are from Gregory *et al.*²⁶ and the Re_c in the experiment was $= 2.8 \times 10^6$. The boundary

layers were tripped in the experiment at $x/c = 0.05$ on the top and bottom surfaces of the airfoil. Boundary layers are therefore also tripped in both FDL3DI and XFOIL simulations at the same location.

The FDL3DI predicted C_p distribution agrees very well with the measured data over the entire airfoil except for the notch in the FDL3DI result due to the trip wire. Since the simulation is at a much lower $Re_c (= 5 \times 10^5)$, the height of the trip wire ($\approx y^+ = 20$) is larger than that used in the experiment to ensure boundary layer transition. XFOIL is run at the same Re_c as FDL3DI with trips located at $x/c = 0.05$. XFOIL does remarkably well in predicting the C_p distribution. Unfortunately, Gregory *et al.*²⁶ does not report measurements of skin friction coefficient, C_f . Given the lack of measured data, FDL3DI predictions are compared against XFOIL predictions in Fig. 10 (b) for C_f distribution over the airfoil surface. Large differences are observed near the trip wire location ($x/c = 0.05$) as expected. In FDL3DI, the trip triggers an instability wave that induces transition over a finite distance, while in XFOIL the transition is instantaneous. Despite this difference, the two predictions agree reasonably well in the aft portion of the airfoil once the transition is complete and the boundary layer is fully turbulent in the FDL3DI simulation.

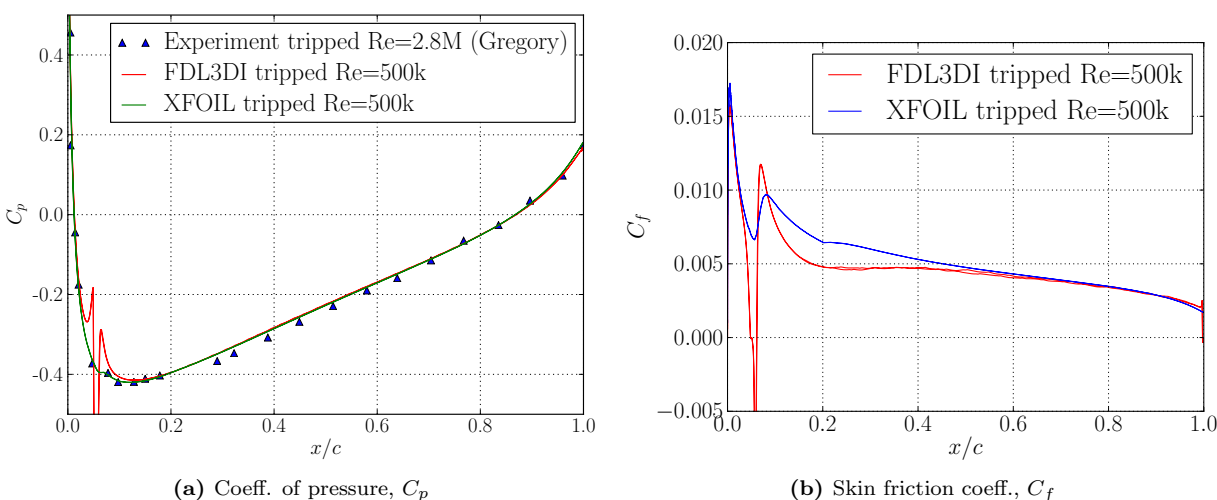


Figure 10. Time- and span-averaged C_p and C_f distributions from FDL3DI predictions ($Re_c = 5 \times 10^5$ with a trip wire) compared with experiments ($Re_c = 2.1 \times 10^6$) and XFOIL simulations ($Re_c = 5 \times 10^5$ with a trip).

2. Baseline v/s Fence Geometry

Time-averaged data from the 3-D simulation of the fence geometry is collected after the flow transients are removed. Figure 11 compares the time- and span-averaged C_p and C_f distributions over the airfoil surface between the baseline and fence geometries. Outside of the fence region, the C_p and C_f distributions are nearly identical between the baseline and fence simulations. The “kinks” in the C_p and C_f distributions near the fence leading edge in the simulations are due to the orthogonal leading edge, and are not expected in the experiments. Within the fence region, both C_p and C_f drop below the corresponding baseline values,

indicating that the flow velocity and velocity shear near the surface are reduced due to the fences. These features are characteristic of forest canopy flows.

The results in Fig. 11 show that the addition of the fences does not adversely affect the aerodynamic performance of the airfoil. Integrated quantities such as sectional drag and lift remain nearly unchanged due to the finlet fence design.

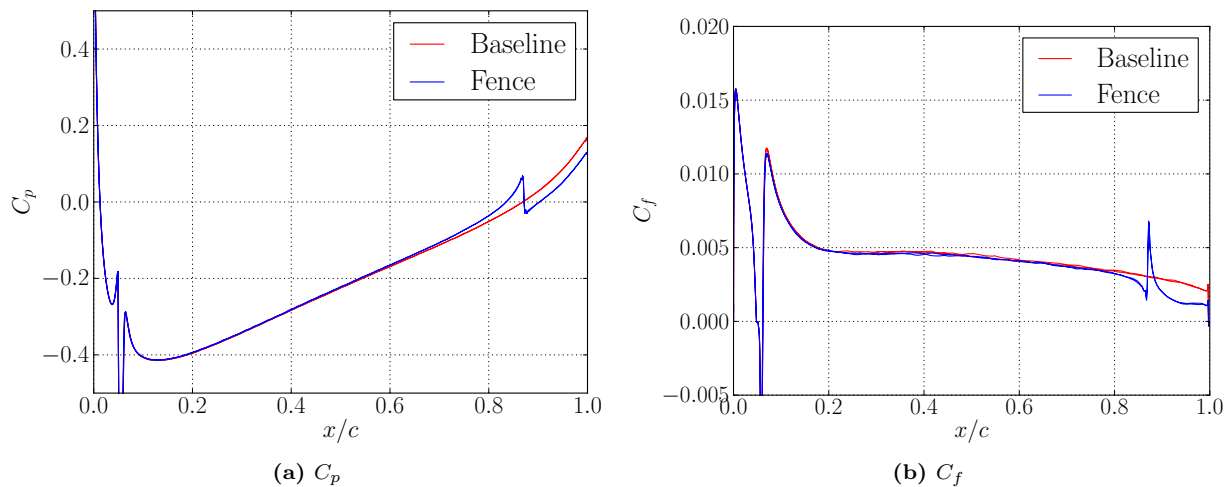


Figure 11. Time- and span-averaged C_p and C_f distributions compared between the baseline and fence simulations with forced transition.

D. Surface Pressure Spectra

The primary noise generation mechanism in this low Mach number flow is the scattering into radiating sound of the hydrodynamic energy in the boundary layer turbulence by the airfoil trailing edge. Unsteady surface pressure near the trailing edge is therefore a measure of noise source strength. Numerical data is collected for approximately $4 \times \tau$ for the spectral analysis and other results presented in this section and the following sections. Surface pressure spectra are computed at the trailing edge ($x/c = 1$). The spectra are averaged over the span; the points that lie within the fences are removed in the averaging procedures for the fence simulation. Figure 12 (a) compares the two numerically-predicted spectra. A measurable reduction at high frequencies and a small increase at low frequencies are observed in the surface pressure spectra with the fence geometry. These observations in the simulations are compared with the *farfield* sound pressure spectra measured using acoustic beamforming.²² *Qualitative* comparisons between measured farfield sound and predicted surface pressure spectra are made in Fig. 12. The figures show that the predictions agree qualitatively with the reductions observed in the measurements.

To understand how the integrated high-frequency sound is varying along the chord through the fences,

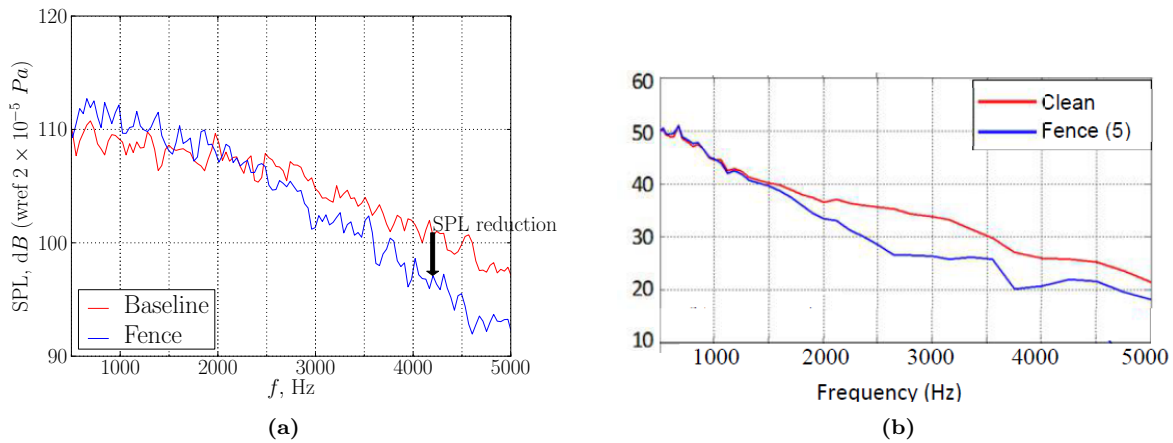


Figure 12. Qualitative comparison between FDL3DI predicted surface pressure spectra and measured farfield acoustic spectra from Ref.²⁰

band sound pressure level (L_{pb}) defined as

$$L_{pb} = 10 \log_{10} \sum_{f_{\min}}^{f_{\max}} (|\hat{p}(f_i)|/p_{ref})^2 \quad (4)$$

is computed. In Eq. 4, f_{\min} and f_{\max} correspond to the indices of the minimum and maximum frequency of the band level over which the spectra is integrated; we integrate over the frequency range $2.5 \text{ kHz} \leq f \leq 5 \text{ kHz}$. The results of the integrated band pressure level are plotted in Fig. 13. The fence geometry has slightly lower L_{pb} from the trailing edge up to $x/c \approx 0.9$. Near the leading edge of the fences however, the band pressure level in the fence geometry is higher. The largest predicted reduction in L_{pb} is observed to be about 3.0 dB at the airfoil trailing edge.

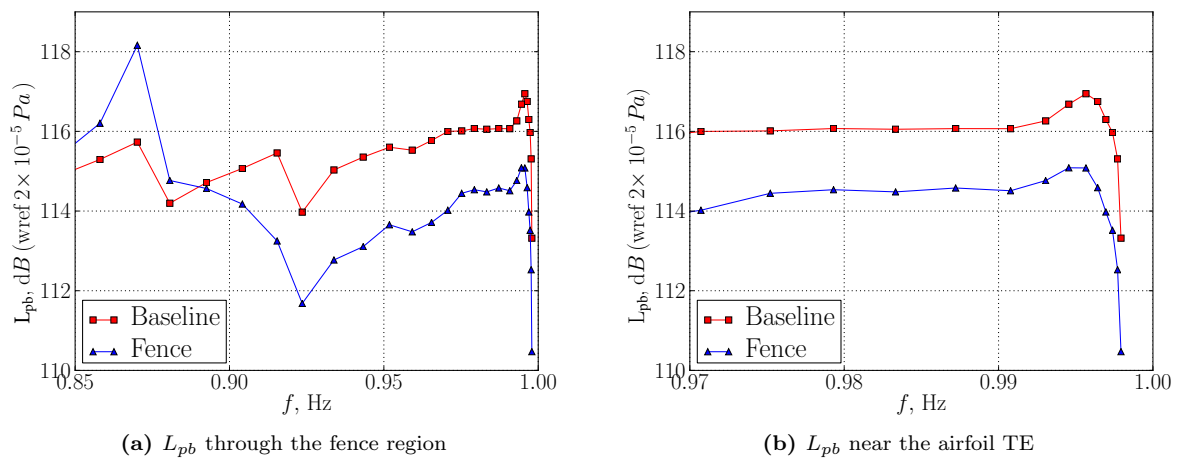


Figure 13. Predicted band pressure level (L_{pb}) on the airfoil surfaces compared between the baseline and fence simulations: (a) in the fence region and (b) near the airfoil trailing edge.

E. Noise Reduction Mechanisms

Two hypotheses are put forth to explain the experimentally observed farfield noise reduction: (1) fences reduce the spanwise correlation length, and (2) fences lift the turbulence eddies away from the scattering (airfoil trailing) edge. These hypotheses are investigated using the simulation results here.

Surface unsteady pressure reduction observed in the simulations (and experiments) is expected to lead to farfield noise reduction based on Amiet's theory.²⁷ Per Amiet,²⁷ trailing edge noise radiated by an airfoil is directly proportional to the spanwise correlation length. Spanwise coherence in the simulations is therefore investigated. The spatial coherence between two points \mathbf{x} and \mathbf{y} is defined as

$$\gamma_{xy}^2(\omega) = \frac{|S_{xy}(\omega)|^2}{S_{xx}(\omega)S_{yy}(\omega)}, \quad (5)$$

where $S_{xx}(\omega)$ is $S_{pp}(\omega)$ evaluated at point \mathbf{x} and $S_{yy}(\omega)$ is $S_{pp}(\omega)$ evaluated at point \mathbf{y} , where \mathbf{x} and \mathbf{y} are points at a given chordwise location but separated in the spanwise direction. The spanwise coherence for the baseline and fence simulations are computed using Eq. 5 along the airfoil trailing edge and plotted in Fig. 14. A visual inspection of the contour plots does not reveal any significant differences in coherence between the baseline and fence geometries.

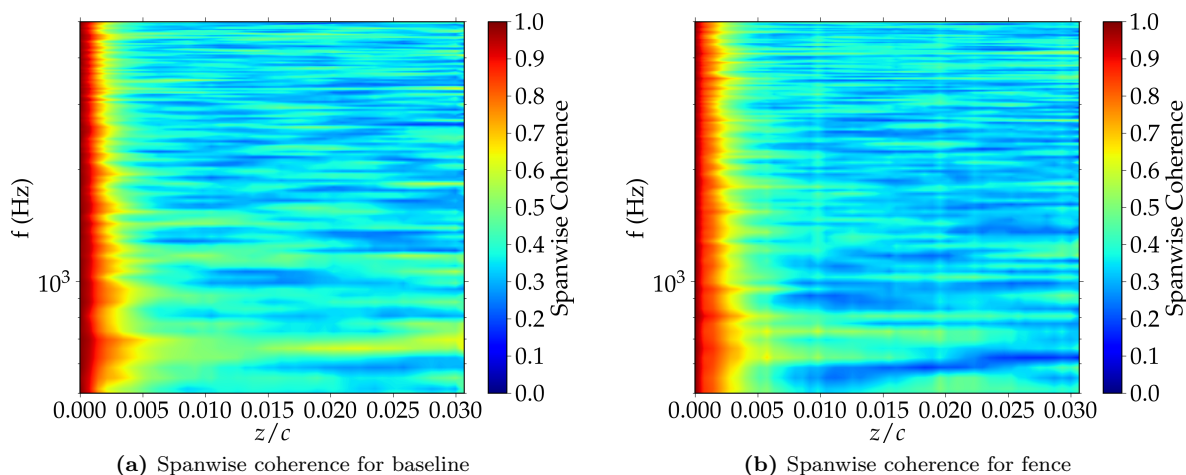


Figure 14. Compressible LES results for NACA 0012 cross section with forced transition, $Re_c = 5 \times 10^5$ showing a) spanwise coherence for baseline and b) spanwise coherence for the fences.

Contour plots of normalized turbulence kinetic energy are compared between the baseline and fence simulations at two different cross-stream planes in Fig. 15. The figures shows isometric views with the back spanwise periodic boundary shown along with the cut plane. The first plane at $x/c = 0.832$ is upstream of the fences. At this location, the TKE is seen concentrated in the boundary layer close to the airfoil surface for both the airfoils. However, at the airfoil trailing edge (see Fig. 15 c&d), the turbulence close to the

airfoil surface (trailing edge) is substantially reduced with the fences, and appears to be concentrated above the fences. The figure clearly indicates that the separation distance between the source (unsteadiness in the turbulence) and the scattering airfoil trailing edge is increased.

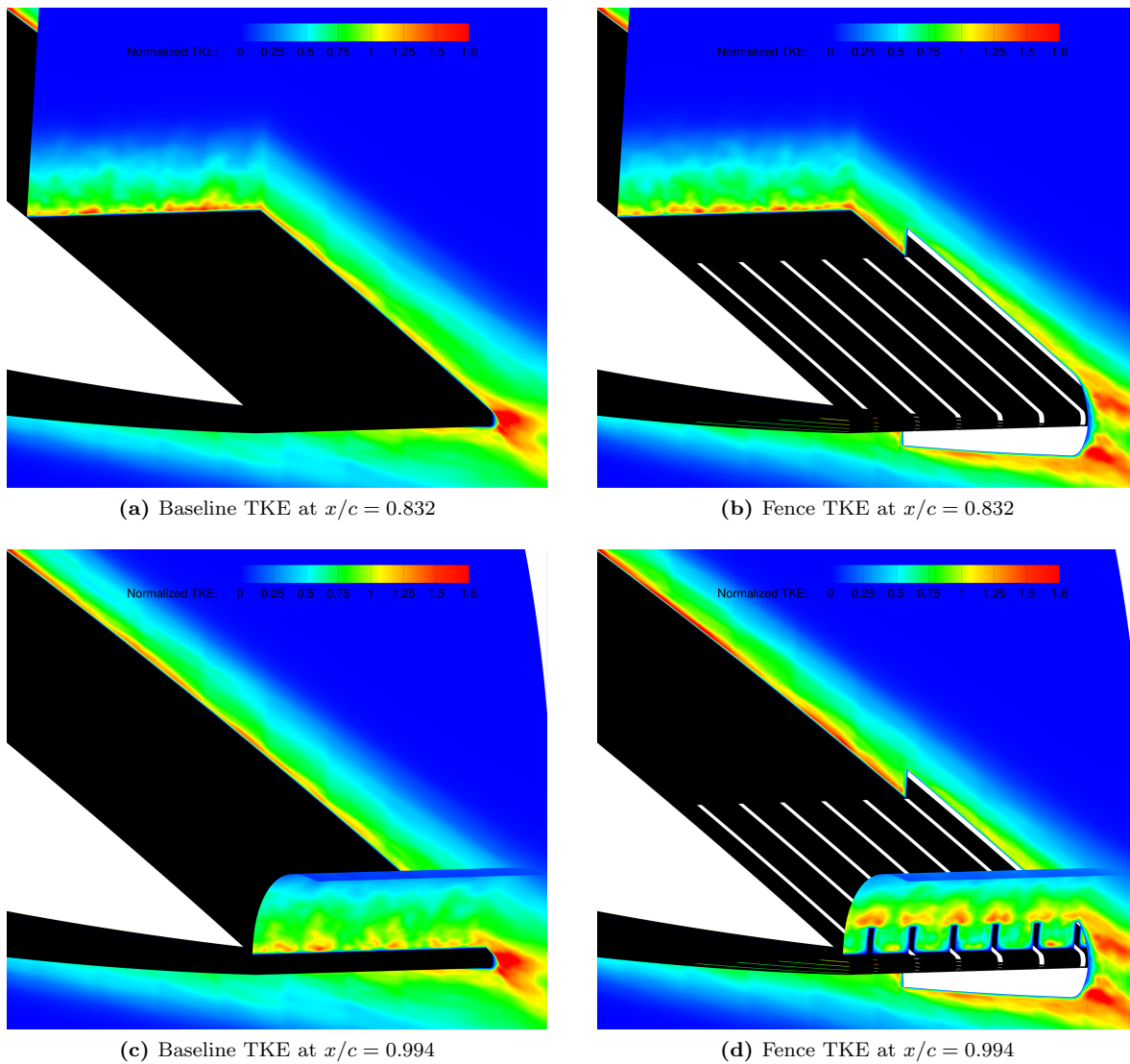


Figure 15. Normalized turbulent kinetic energy (k/u^{*2}) for the baseline and fence simulations: (a & b) upstream of the fence at $x/c = 0.832$, and (c & d) near the airfoil trailing edge at $x/c = 0.994$.

Figure 16 compares the span-averaged TKE profiles between the baseline and the fence geometries at the two cross-stream locations corresponding to the plots in Fig. 15. The line plots quantitatively show the reduction in TKE near the surface and concentration of TKE above the fences; the ordinate in Fig. 15 is normalized by the fence height. These results substantiate the second hypothesis for the observed reduction in unsteady surface pressure and farfield noise.

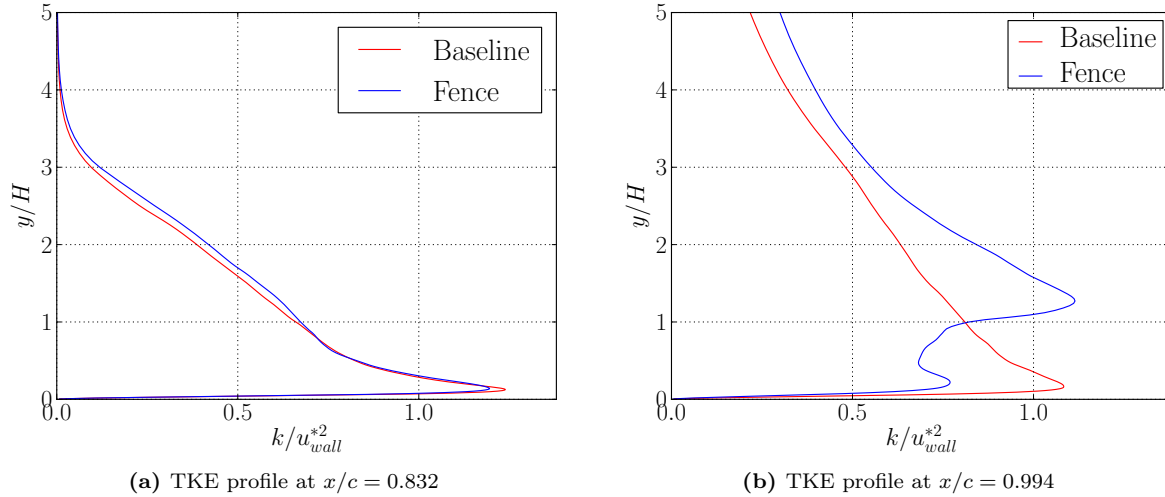


Figure 16. Span-averaged normalized turbulent kinetic energy (k/u^{*2}) profiles compared between the baseline and fence simulations: (a) upstream of the fence at $x/c = 0.832$, and (b) near the airfoil trailing edge at $x/c = 0.994$.

V. Conclusions

This paper presents numerical investigations of airfoil geometries inspired by the soft down coat of the owl. Large eddy simulations are performed for the baseline (NACA 0012) airfoil and an owl-inspired airfoil (with fences). The solver uses sixth-order spatial differencing, second order implicit time integration, and spatial filtering to remove unresolved wavenumbers. The following conclusions are drawn from the study:

1. Comparisons of time- and span-averaged C_p and C_f distributions show that the fences inspired by the owl down coat do not significantly alter the aerodynamic performance of the baseline airfoil.
2. Comparison of surface pressure spectra between the baseline and fence airfoils show a reduction at high frequencies and a slight increase in the low frequencies near the airfoil trailing edge. Band pressure level, obtained by integrating over the high frequencies, show a reduction of up to 3.0 dB near the airfoil trailing edge.
3. Two hypothesis for the observed reduction (in previous experiments) in farfield sound are evaluated:
 - (a) Comparison of spanwise coherence contour plots between the baseline and fence geometries at the airfoil trailing edge shows no significant differences, which suggests that spanwise correlation is not reduced due to the fences and hence is not responsible for the observed farfield noise reduction.
 - (b) Normalized turbulence kinetic energy (TKE) contour plots and span-averaged profiles clearly show a redistribution of TKE away from the airfoil trailing edge.

The simulation results show that the primary reason for the observed noise reduction with fences in the experiments is likely due to the increased source-scattering edge separation distance, which makes the scattering process inefficient. In the future, more noise source diagnostics will be carried out and far field noise propagation will be performed using integral methods such as the Ffowcs Williams-Hawkings acoustic analogy.

Acknowledgments

This research is funded by the National Science Foundation under grant number NSF/ CBET-1554196. Computational resources used for this research are provided by NSF XSEDE (Grant # TG-CTS130004) and the Argonne Leadership Computing Facility, which is a DOE Office of Science User Facility supported under Contract DE-AC02-06CH11357. Technical support for the FDL3DI software provided by Dr. Daniel Garmann of Air Force Research Laboratory is acknowledged. Funding through the Wind Energy Science, Engineering, and Policy program is also acknowledged.

References

- ¹Passchier-Vermeer, W. and Passchier, W. F., “Noise exposure and public health,” *Environ Health Perspect*, Vol. 108, No. 1, 2000, pp. 123–31.
- ²Franssen, E. A. M., van Wiechen, C. M. A. G., Nagelkerke, N. J. D., and Lebet, E., “Aircraft noise around a large international airport and its impact on general health and medication use,” *Occup Environ Med*, Vol. 61, No. 5, 2004, pp. 405–413.
- ³Morrell, S., Taylor, R., and Lyle, D., “A review of health effects of aircraft noise,” *Australian and New Zealand Journal of Public Health*, Vol. 21, No. 2, 1997, pp. 221–36.
- ⁴Farboud, A., Crunkhorn, R., and Trinidad, A., “‘Wind turbine syndrome’: fact or fiction?” *J Laryngol Otol*, Vol. 127, No. 3, 2013, pp. 222–226.
- ⁵Pedersen, E. and Waye, K. P., “Perception and annoyance due to wind turbine noise—a dose-response relationship,” *Journal of the Acoustical Society of America*, Vol. 116, No. 6, 2004, pp. 3460–3470.
- ⁶Benyus, J. M., *Biomimicry: Innovation inspired by nature*, William Morrow Paperbacks, 2002.
- ⁷Kroeger, R. A., Grushka, H. D., and Helvey, T. C., “Low speed aerodynamics for ultra-quiet flight,” Tech. rep., Wright-Patterson Air Force Base, 1972.
- ⁸Hersh, A. S., Sodermant, P. T., and Hayden, R. E., “Investigation of Acoustic Effects of Leading-Edge Serrations on Airfoils,” *Journal of Aircraft*, Vol. 11, No. 4, 1974, pp. 197–202.
- ⁹Soderman, P. T., “Leading Edge Serrations which Reduce the Noise of Low-Speed Rotors,” Tech. Rep. NASA-TN-D-7371, NASA Ames Research Center, 1983.
- ¹⁰Sandberg, R. D. and Jones, L. E., “Direct numerical simulations of low Reynolds number flow over airfoils with trailing-edge serrations,” *Journal of Sound and Vibration*, Vol. 330, No. 16, 2011, pp. 3818–3831.
- ¹¹Roger, M., Schram, C., and De Santana, L., “Reduction of Airfoil Turbulence-Impingement Noise by Means of Leading-

Edge Serrations and/or Porous Material,” *19th AIAA/CEAS Aeroacoustics Conference*, American Institute of Aeronautics and Astronautics, 2013.

¹²Agrawal, B. R. and Sharma, A., “Numerical analysis of aerodynamic noise mitigation via leading edge serrations for a rodairfoil configuration.” *International Journal of Aeroacoustics*, Vol. 15, No. 8, 2016, pp. 734–756.

¹³Jaworski, J. W. and Peake, N., “Aerodynamic noise from a poroelastic edge with implications for the silent flight of owls,” *Journal of Fluid Mechanics*, Vol. 723, 2013, pp. 456–479.

¹⁴Geyer, T., Sarradj, E., and Fritzsche, C., “Measurement of the noise generation at the trailing edge of porous airfoils,” *Experiments in Fluids*, Vol. 48, No. 2, 2010, pp. 291–308.

¹⁵Narayanan, S., Chaitanya, P., Haeri, S., Joseph, P., Kim, J. W., and Polacsek, C., “Airfoil noise reductions through leading edge serrations,” *Physics of Fluids*, Vol. 27, No. 2, 2015.

¹⁶Oerlemans, S., Fisher, M., Maeder, T., and Kgler, K., “Reduction of Wind Turbine Noise Using Optimized Airfoils and Trailing-Edge Serrations,” *AIAA Journal*, Vol. 47, No. 6, 2009, pp. 1470–1481.

¹⁷Jaworski, J. and Peake, N., “Vortex Noise Reductions from a Flexible Fiber Model of Owl Down,” 2013.

¹⁸Cavalieri, A. V., Wolf, W. R., and Jaworski, J., “Acoustic scattering by finite poroelastic plates,” *20th AIAA/CEAS Aeroacoustics Conference*, AIAA Aviation, American Institute of Aeronautics and Astronautics, 2014.

¹⁹Clark, I. A., Devenport, W., Jaworski, J. W., Daly, C., Peake, N., and Glegg, S., “Noise Generating and Suppressing Characteristics of Bio-Inspired Rough Surfaces,” *20th AIAA/CEAS Aeroacoustics Meeting*, American Institute of Aeronautics and Astronautics, 2014.

²⁰Clark, I. A., Alexander, N. W., Devenport, W., Glegg, S., Jaworski, J. W., Daly, C., and Peake, N., “Bioinspired Trailing-Edge Noise Control,” *AIAA Journal*, Vol. 55, No. 3, 2017, pp. 740–754.

²¹Clark, I. A., Devenport, W., Jaworski, J. W., Daly, C., Peake, N., and Glegg, S., “Bio-Inspired Trailing Edge Noise Control,” *21st AIAA/CEAS Aeroacoustics Conference*, American Institute of Aeronautics and Astronautics, 2015.

²²Dougherty, R., “Extensions of DAMAS and benefits and limitations of deconvolution in beamforming,” *11th AIAA/CEAS aeroacoustics conference*, 2005, p. 2961.

²³Visbal, R. M. and Gaitonde, V. D., “On the Use of Higher-Order Finite-Difference Schemes on Curvilinear and Deforming Meshes,” *Journal of Computational Physics*, Vol. 181, No. 1, 2002, pp. 155–185.

²⁴Visbal, M. R. and Rizzetta, D. P., “Large-Eddy Simulation on Curvilinear Grids Using Compact Differencing and Filtering Schemes,” *Journal of Fluids Engineering*, Vol. 124, No. 4, 2002, pp. 836.

²⁵Drela, M., “XFOIL: An analysis and design system for low Reynolds number airfoils,” *Low Reynolds number aerodynamics*, Springer, 1989, pp. 1–12.

²⁶Gregory, N. and O’Reilly, C. L., “Low-Speed Aerodynamic Characteristics of NACA 0012 Aerofoil Section, including the Effects of Upper-Surface Roughness Simulating Hoar Frost,” Tech. Rep. NASA Reports and Memoranda 3726, 1970.

²⁷Amiet, R. K., “Acoustic radiation from an airfoil in a turbulent stream,” *Journal of Sound and Vibration*, Vol. 41, No. 4, 1975, pp. 407–420.